Pulsed-laser lensing for phase modulation in electron microscopy

Daniel X. Du[1,2,3], Adam C. Bartnik[4], Cameron J. R. Duncan[5], Usama Choudhry[6], Tanya Tabachnik[1], Chaim Sallah[1], Yuki Ogawa[1,2,3], Ebrahim Najafi[7], Ding-Shyue Yang[8], Jared M. Maxson[4*] & Anthony W. P. Fitzpatrick[1,2,3*]

[1] Mortimer B. Zuckerman Mind Brain Behavior Institute, Columbia University, New York, NY 10027, USA.

[2] Department of Biochemistry and Molecular Biophysics, Columbia University, New York, NY 10032, USA.

[3] Taub Institute for Research on Alzheimer's Disease and the Aging Brain, Columbia University Irving Medical Center, 630 West 168th Street, New York, NY 10032, USA.

[4] Cornell Laboratory for Accelerator-Based Sciences and Education, Cornell University, Ithaca, New York, NY 14853, USA

[5] Università degli Studi di Milano-Bicocca, Milan, Italy

[6] Department of Mechanical Engineering, University of California, Santa Barbara, CA 93106, USA

[7] The Chemours Company, Wilmington, DE 19899, USA

[8] Department of Chemistry, University of Houston, Houston, TX 77204, USA

*e-mail: jmm586@cornell.edu; Anthony.Fitzpatrick@columbia.edu

Abstract

Phase contrast electron microscopy is fundamental for visualizing unstained biological specimens. Advances in electron detection have not yet overcome the low contrast caused by weak scattering. Here, we demonstrate that an orthogonal pulsed laser-electron beam interaction produces a pronounced phase shift through ponderomotive defocusing. With focus-tracking external optics, pulsed-laser lensing of the electron beam has the potential to simultaneously enhance phase contrast and correct aberrations in cryo-electron tomography.

Almost a century ago, magnetic lenses were first incorporated into an electron microscope[1]. Since then, electron microscopy has advanced from barely surpassing the optical diffraction limit[2] to employing aberration corrected lenses that resolve features smaller than fifty picometers[3], close to the Bohr radius of a hydrogen atom. These extraordinary gains in precision, stability, and versatility underpin many imaging breakthroughs in materials science[3], nanotechnology[4], and structural biology[5].

Beyond static magnetic fields, electron beams can also be manipulated by time-varying electromagnetic fields such as laser pulses. Recent work shows that the optical field of a laser can be used to shape the beam[6] or impose precise phase shifts[7]. Deflecting a 300 kV electron beam with light requires peak optical intensities on the order of GW/cm^2 [8]. Such extreme intensities are most readily obtained with ultrafast laser pulses[9]. For example, compressing just ten microjoules of laser energy into a pulse lasting only ten femtoseconds generates an instantaneous power of one gigawatt.

Here, we conduct stroboscopic ultrafast experiments that demonstrate how an orthogonally traveling pulsed laser beam, which is introduced into the microscope through standard optical windows, can induce pronounced spatial lensing of electron packet trajectories (Fig. 1a). The pulsed-laser lensing corresponds directly to phase shifts in the electron wavefront. This proof-of-concept experiment demonstrates that externally tuned, microjoule laser pulses can induce ponderomotive phase shifts exceeding hundreds of radians. This surpasses the $\pi/2$ radian threshold required for maximum-contrast cryo-electron microscopy[8] by two orders of magnitude, pushing laser-electron interactions into a classical regime where beam deflection becomes readily observable.

To demonstrate elastic interactions between a pulsed laser beam and strobed electron packets, we generate photoelectrons (electron energy 30 kV, pulse duration of 6.8 ± 0.9 ps) with femtosecond ultraviolet (UV) pulses (0.5 nJ/pulse, 500 fs fwhm, 1 MHz repetition rate) from a

zirconium-coated tungsten tip and intersect them orthogonally with green laser pulses (λ=512 nm). The interaction volume is approximately 14 × 14 × 14 μm^3. We measure the ponderomotive defocusing of the electrons by imaging 290 nm holes in a gold foil and observing the resulting change in beam distribution. The induced phase shifts are large enough that the corresponding momentum changes are detectable, as the ponderomotive effect pushes the electron wavefunction away from the region of highest photon density. We determine the phase shift imparted to the electron beam by correlating experimental data to simulated data. The electron beam parameters (astigmatism, defocus, rotation, resolution, and counts) were optimized to maximize the number of momentum-shifted electrons that could be detected (Supplementary Table S1). Details on laser (Fig. S1) and electron beam (Fig. S2) sizes are provided in the Supplementary Information.

Although we drive the quantum-mechanical phase shift into the hundreds-of-radians regime, the ponderomotive intensity modulation of the beam remains faint. To detect it, we subtract micrographs taken without electron-laser interaction from those recorded at time zero; the exact moment when electron packets and pulsed photons interact directly. These noise-filtered difference images of single holes (Fig. 1b, *top*) are compared with simulated difference images (Fig. 1b, *bottom* and Supplementary Note 1). Due to the astigmatism and rotation of the electron beam resulting from lens alignments (Supplementary Table S1), the ponderomotive effect deflects the electrons along an axis 41° from the normal to the laser beam's propagation direction (Fig. 1b, *top*). Counts integrated along this line are plotted (Fig. 1c, filled yellow circles). Significantly, the ponderomotive effect of the pulsed laser defocuses the electron beam, producing a transverse shift of approximately one micron (Fig. 1c, filled yellow circles). The smaller lobe to the bottom left has diminished intensity and the electrons are pushed into the top right corner, with a peak difference intensity of 1.5% (Figs. 1b, *top* and 1c). The simulated image provides a similar shape profile (Fig. 1b, *bottom*), but the predicted signal is somewhat muted, suggesting the effect is stronger than expected (Fig. 1c, dashed

line). The discrepancy likely arises from an overestimation of the electron-packet pulse duration, as shorter packets would generate a stronger signal.

In a second experiment focused on the stability of the effect, we acquired 4,200 consecutive difference images (Figure 1d). Over the 10-hour measurement period, the effect varies by less than 10% from its mean value, which is -1.27% ± 0.13% (Figure 1d, filled yellow circles). Difference images recorded when the laser and electron beam do not interact converge to a mean difference intensity of zero, as expected (Figure 1d, filled blue circles). This data demonstrates that the effect is stable for long periods of time, provided that no external factors result in a spatial misalignment of either beam. Figure S3 presents a control experiment confirming that the results are independent of stage position and not an artefact arising from spurious interactions between the laser, electrons, and sample.

To probe how the ponderomotive effect varies with electron-pulse length, we tuned the pulse duration by changing the UV excitation energy. Lower UV energies produce shorter electron packets that carry fewer electrons, which lessens space-charge repulsion and improves beam coherence[10]. At a UV pulse energy of 0.25 nJ, the electrons form packets only 5.8 ± 1.9 ps long and exhibit the largest intensity change, −4.1 ± 1.1% (Fig. 2a, *top*). Increasing the UV pulse energy to 0.5 nJ stretches the pulse to 7.1 ± 1.1 ps and lowers the intensity change to −3.3 ± 0.2%, averaged over two measurements (Fig. 2a, *middle*). Further increasing the pulse energy to 1.0 nJ lengthens the electron packet to 13.4 ± 0.9 ps, with the intensity change falling to −3.0 ± 0.1% (Fig. 2a, *bottom*). Thus, raising the UV energy from 0.25 nJ to 1.0 nJ more than doubles the electron-pulse duration while the magnitude of the intensity difference steadily decreases.

Beyond electron-pulse duration, spatial precision proves equally critical for maximizing the ponderomotive effect. The intensity modulation peaks sharply within the narrow ~20 μm interaction

zone (Figs. S1, S2) where the electron and laser beams intersect (Fig. 2b), underscoring that our precise alignment maximizes the interaction strength. This spatial sensitivity, combined with the pulse duration dependence, establishes that optimal ponderomotive coupling requires both ultrashort electron pulses and precise beam overlap.

To quantify the momentum and phase shifts generated by the ponderomotive effect, we use an analytical model[6] for the case of orthogonal beams, where the electric field of the laser takes the form:

$$(1)\ \underline{A}(\underline{r},t) = -\frac{\epsilon_0 \hat{y}}{\omega_L} g(y,z) \sin\left[\omega_L\left(t-\frac{x}{c}\right)\right] u\left(t-\frac{x}{c}\right)$$

Here, c, and ϵ_0 are universal constants, $g(y,z)$ is the gaussian profile of the laser beam, and ω_L is the frequency of the light. We derive the momentum shift from $\delta\underline{p} = \hbar\nabla\phi(\underline{r},t)$ (see Supplementary Note 1). Using the characterized electron beam parameters (Supplementary Table S1), we observe the expected cylindrical-like concave lens behavior, with a focal length of approximately -42 ± 14 mm.

By optimizing the match between the experimental and simulated difference images (Fig. 1b), we extract the experimental parameters and compute the momentum kick imparted by the pulsed ponderomotive potential to the electron beam (Fig. 2c and Supplementary Note 1). The magnitude of the resulting momentum shift, approximately 90 μrad, is strongly anisotropic and lies mainly along the major axis of the black ellipse bounding the electron beam in Fig. 2c. Converting the measured momentum shift to its equivalent phase (see Supplementary Note 1) reveals that the ponderomotive interaction imposes a peak phase of roughly 430 radians on the electron beam (Fig. 2d), which far exceeds the required π/2 radians for phase interference.

In conclusion, we demonstrate that even femtosecond, microjoule laser pulses, introduced orthogonally to a pulsed electron beam, can serve as a tunable ponderomotive lens (Fig. 1a)[11]. This free-space interaction imposes phase shifts of roughly 400 rad (Fig. 2d), greatly in excess of the $\pi/2$ threshold for strong interference, and imparts a stable momentum kick of approximately 90 μrad (Fig. 2c) that is stable for many hours (Fig. 1d). The lensing strength scales with electron-pulse duration (Fig. 2a) and beam overlap (Fig. 2b), establishing clear experimental guidelines for optimum coupling in a transmission electron microscope[9,12]. With all parameters adjustable outside the electron microscope[13], this approach introduces a flexible, contact-free laser lensing technique that augments conventional electron optics. External optics allow the pulsed-laser phase plate to precisely shift its focus, keeping the laser-electron interaction aligned with the moving back-focal-plane crossover during sample tilting in cryo-electron tomography[14], thus preserving optimal phase contrast and image quality. In addition to enhancing phase contrast in cryo-electron tomography[7,8], tailored laser fields could correct residual aberrations in real time[15], narrow the energy spread for improved monochromaticity[16], or provide adaptive beam shaping for ptychography[17] or relativistic electron optics[18]. Laser-based lensing thus provides a versatile approach for all-optical aberration correction and dynamic beam conditioning, enhancing and expanding the capabilities of traditional electron microscopes.

Methods

Pulsed ponderomotive electron lensing experiment

The experiment consists of a pulsed laser and scanning electron microscope. The laser is an NKT Photonics Aeropulse FS20-050 operating a fundamental wavelength of 1030 nm and frequency doubled with a second-harmonic-generation module to 515 nm. The output power is 9W. The repetition rate of the experiment is set to 1 MHz for optimum power-per-pulse. The beam is initially passed through a 90:10 beam splitter. The weaker leg (probe) is further frequency doubled to 257 nm and modulated with waveplates and polarizers to generate photoelectrons at the ZrO coated

tungsten FEG tip cathode *via* the photoelectric effect[19,20]. To synchronize the laser pulse with the electron pulses, the stronger leg (pump) is delayed with a retroreflector and motion stage (mks IDL225-600LM). Due to spurious losses on the table from reflections and transmission, only 3.2 W of pump light enters the SEM. Once within the SEM, the pump is focused into the electron-photon interaction zone with a waist diameter of 12.5 μm (Fig. S1).

The microscope is a TFS Nova NanoSEM and, in photoelectron mode, operates at 30 keV accelerating voltage, 0.1 A tip current, and 1230 V in the C1 lens. A 1000 μm aperture is used to optimize the beam current, simultaneously setting the electron beam size to 12-24 microns at the interaction zone (Fig. S2). The airbags were disabled to ensure laser positional stability, with less than 5 microns of drift after 7 days of experimentation. A standard silicon photoexcitation experiment was performed to identify the temporal overlap between electron and laser pulses on the delay stage[19,20]. To ensure no side-lobes were produced for each electron pulse, the optical port originally at the cathode was replaced with a UV anti-reflective-coated window (TSL VPZ16QBBAR). To prevent the pump light from saturating the Everhart-Thornley Detector, a spectral filter (Asahi Spectra XVS0490 shortpass 490 nm) was fixed behind the light-pipe.

The holey gold spatial filter (Quantafoil HexAuFoil) with 290 nm holes is conductively bound to a degenerate p-type B-doped silicon (MTI Corporation, < 5 Å roughness, 0.001-0.005 Ω·cm resistivity) platform serving as a smooth conductive dark background and settled (10 mm) 7mm below the (polepiece) ponderomotive interaction zone. Images were collected at 10,000× to 20,000× magnification and in a narrowed region of interest encapsulating one unit cell of the repeating holey pattern. Each acquisition was subtracted against a reference timepoint after drift correction. A second reference timepoint was acquired to serve as a control. This establishes the differences at time-zero are statistically different from any noise in the reference images, as is clearly shown in Figure 1d. A second control was performed by physically moving the specimen such that, if the effect was related to some surface phenomena, time-zero would also move. No shift in time-zero was observed and the result of this experiment is shown in Figure S3.

References

1. Ruska, E. & Knoll, M. Die magnetische Sammelspule für schnelle Elektronenstrahlen. *Z. techn. Physik*. **12**, 389-400 & 448 (1931).
2. M. Knoll, M. & Ruska, E. Das Elektronenmikroskop. *Z. Physik*. **78**, 318-339 (1932).
3. Chen Z, *et al*. Electron ptychography achieves atomic-resolution limits set by lattice vibrations. *Science* **372**, 826-831 (2021).
4. Meyer, J. C., Geim, A. K., Katsnelson, M. I., Novoselov, K. S., Obergfell, D., & Roth, S. The structure of suspended graphene sheets. *Nature* **446**, 60-63 (2007).
5. Nakane, T. *et al*. Single-particle cryo-EM at atomic resolution. *Nature* **587**, 152-156. (2020).
6. Mihaila, M. C. C., *et al*. Transverse Electron-Beam Shaping with Light. *Phys. Rev. X* **12**, 031043 (2022).
7. Schwartz, O. *et al*. Laser phase plate for transmission electron microscopy. *Nature Methods* **16**, 1016-1020 (2019).
8. Turnbaugh, C., *et al*. High-power near-concentric Fabry-Perot cavity for phase contrast electron microscopy. *Rev Sci Instrum*. **92**, 053005 (2021).
9. Du, D. X. & Fitzpatrick, A. W. P. Design of an ultrafast pulsed ponderomotive phase plate for cryo-electron tomography. *Cell Reports Methods* **3**, 100387 (2023).
10. Feist, A., *et al*. Ultrafast transmission electron microscopy using a laser-driven field emitter: Femtosecond resolution with a high coherence electron beam. *Ultramicroscopy* **176**, 63-73 (2017).
11. Reed, B. W. Ponderomotive phase plate for transmission electron microscopes. (Lawrence Livermore National Lab (LLNL), Livermore, CA (United States), 2012).
12. van Leeuwen, K. *et al*. Feasibility of a pulsed ponderomotive phase plate for electron beams. *New Journal of Physics* **25**, 023031 (2023).
13. Fitzpatrick, A. W. P., Lorenz, U. J., Vanacore, G. M., Zewail, A. H. 4D cryo-electron microscopy of proteins. *J Am Chem Soc*. **135**, 19123-19126 (2013).
14. Lucić, V., Förster, F., & Baumeister, W. Structural studies by electron tomography: from cells to molecules. *Annual Review of Biochemistry* **74**, 833-865 (2005).
15. Mihaila, M. C. C., Streshkova, N.L. & Kozák, M. Light-Based Chromatic Aberration Correction of Ultrafast Electron Microscopes. *Phys. Rev. Lett*. **134**, 203802 (2025).
16. Duncan, C. J. R., Muller, D. A. & Maxson, J. M. Lossless Monochromation for Electron Microscopy with Pulsed Photoemission Sources and Radio-Frequency Cavities. *Phys. Rev. Applied* **14**, 014060 (2020).
17. Küçükoğlu, B., *et al*. Low-dose cryo-electron ptychography of proteins at sub-nanometer resolution. *Nat Commun*. **15**, 8062 (2024).
18. Feist, A., *et al*. Quantum coherent optical phase modulation in an ultrafast transmission electron microscope. *Nature* **521**, 200-203 (2015).
19. Yang, D.-S., Mohammed, O. F. & Zewail, A. H. Scanning ultrafast electron microscopy. *Proc. Natl. Acad. Sci.* **107**, 14993-14998 (2010).
20. Du, D. X., *et al*. Development of an ultrafast pulsed ponderomotive phase plate for cryo-electron tomography. *bioRxiv* 2024.03.20.585981 (2024).

Acknowledgements

This work was supported by the Chan Zuckerberg Initiative, Visual Proteomics Grant under award no. 2021-234816.

Author contributions

D.X.D., A.C.B., C.J.R.D., E.N., D.Y., J.M.M., and A.W.P.F. conceived the experiments. D.X.D., T.T., C.S., and A.W.P.F. designed and fabricated components. D.X.D. built the optical set-up and carried out the experiments and data analysis, supported by A.C.B., U.C., E.N., D.Y., J.M.M., and A.W.P.F. Y.O. helped prepare figures. The manuscript was written by D.X.D., A.C.B., J.M.M., and A.W.P.F. after discussions with, and input from, all authors. A.W.P.F. supervised the project.

Competing interests

The authors declare no competing financial interests.

Figures

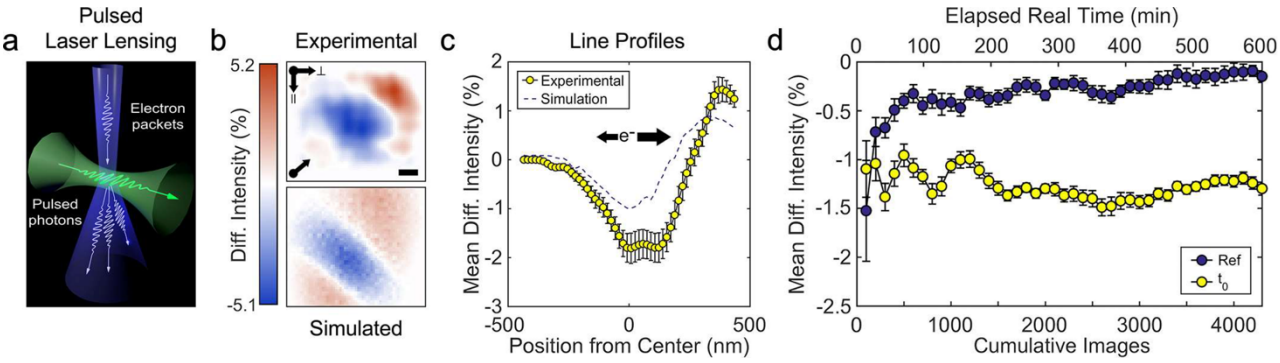

Fig. 1 | Pulsed-laser lensing of an electron beam using the ponderomotive effect. a, A pulsed laser (green) intersects with a strobed electron beam (purple) orthogonally, making each interacting electron packet behave as though it passes through a concave cylindrical lens. The ponderomotive effect of the pulsed laser defocuses the electron beam and simultaneously imposes a phase shift. **b,** Difference images were generated by subtracting the negative-time reference image, acquired 21-67 ps before the photons arrive, from the time-zero image, when the photon pulses overlaps the electron packets. After noise filtering, these experimental difference images (**b**, *top*) are compared with simulated counterparts (**b**, *bottom*). The colorbar indicates the difference intensity in percentage of peak image counts. Axes are provided to indicate directions parallel and perpendicular to the laser Poynting vector. A third arrow is used to show the near-diagonal direction of laser lensing due to the ponderomotive effect. Scale bar, 100 nm. **c,** A line profile of the difference intensity along the axis of pulsed-laser lensing due to the ponderomotive effect. The direction along which electrons are preferentially pushed is indicated by the larger black arrow. Experimental data is shown as filled yellow circles (±S.E.M.) with simulated data shown as a dashed line. **d,** Demonstration of stability of pulsed-laser lensing due to the ponderomotive effect. Filled yellow circles (± S.E.M.) denote the mean difference intensity at time zero, while filled blue circles (± S.E.M.) indicate the mean difference intensity at -21 ps.

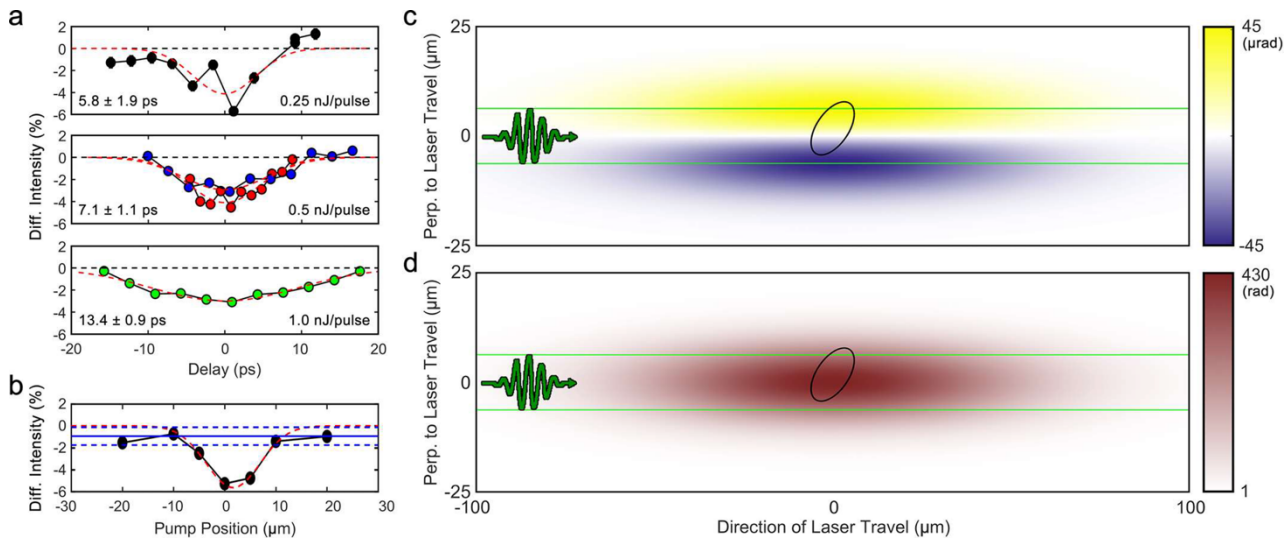

Fig. 2 | Maximizing pulsed-laser lensing by exploiting the ponderomotive effect. a, Increasing the UV pulse energy (*top*, 0.25 nJ/pulse → *middle*, 0.5 nJ/pulse → *bottom*, 1.0 nJ/pulse) lengthens the photoelectron packet (*top*, 5.8 ± 1.9 ps → *middle*, 7.1 ± 1.1 ps → *bottom*, 13.4 ± 0.9 ps). An approximate twofold increase in electron pulse duration weakens the ponderomotive effect, as evidenced by a steady reduction in the intensity difference (*top*, −4.1 ± 1.1% → *middle*, −3.3 ± 0.2% → *bottom*, −3.0 ± 0.1%). **b,** A strong ponderomotive effect requires the pulsed laser and the electron packets to have maximum spatial overlap. Shifting the laser beam perpendicular to its axis illustrates how even slight misalignment weakens the interaction. The solid blue line shows the mean signal in the negative-time reference images, while the flanking dashed blue lines denote its error bounds (± S.E.M.). **c,** Momentum shift (μrad) produced by the ponderomotive effect in the axis orthogonal to both beams. A 500-fs laser pulse (green wave packet, propagating left-to-right) intersects an electron packet that moves into the page (black outline). The continuous green lines mark the 12.5 μm laser-beam diameter, while the black ellipse (major axis ~15 μm) shows the simulated electron-beam profile calculated from the experimental parameters in Supplementary Table S1. **d,** The ponderomotive effect generated by the pulsed laser (green wave packet propagating left-to-right; 12.5 μm beam bounded by solid green lines) imparts an equivalent phase shift of roughly 430 radians to the electron packets traveling into the page (black outline).

Pulsed-laser lensing for phase modulation in electron microscopy

Supplementary Information

Daniel X. Du[1,2,3], Adam C. Bartnik[4], Cameron J. R. Duncan[5], Usama Choudhry[6], Tanya Tabachnik[1], Chaim Sallah[1], Yuki Ogawa[1,2,3], Ebrahim Najafi[7], Ding-Shyue Yang[8], Jared M. Maxson[4*] & Anthony W. P. Fitzpatrick[1,2,3*]

[1] Mortimer B. Zuckerman Mind Brain Behavior Institute, Columbia University, New York, NY 10027, USA.

[2] Department of Biochemistry and Molecular Biophysics, Columbia University, New York, NY 10032, USA.

[3] Taub Institute for Research on Alzheimer's Disease and the Aging Brain, Columbia University Irving Medical Center, 630 West 168th Street, New York, NY 10032, USA.

[4] Cornell Laboratory for Accelerator-Based Sciences and Education, Cornell University, Ithaca, New York, NY 14853, USA

[5] Università degli Studi di Milano-Bicocca, Milan, Italy

[6] Department of Mechanical Engineering, University of California, Santa Barbara, CA 93106, USA

[7] The Chemours Company, Wilmington, DE 19899, USA

[8] Department of Chemistry, University of Houston, Houston, TX 77204, USA

*e-mail: jmm586@cornell.edu; Anthony.Fitzpatrick@columbia.edu

Supplementary Note 1. Simulations

1.1 Derivation

The phase shift (as provided by an integral of the Hamiltonian) is:

$$\phi(\underline{r}) = -\int dt' \frac{1}{\hbar} U(\underline{r}(t'), t')$$

where U is the potential the electron passes through. The interaction potential for the ponderomotive effect is[1]:

$$U(\underline{r}, t) = \frac{e}{2m_e\gamma}\left[A_x^2(\underline{r}(t), t) + A_y^2(\underline{r}(t), t) + \frac{1}{\gamma^2}A_z^2(\underline{r}(t), t)\right] + e\underline{v} \cdot \underline{A}(\underline{r}(t), t) - e\Phi(\underline{r}(t), t)$$

where e and m_e are the constants for the charge and mass of an electron respectively. γ and $\underline{v}$ are the Lorentz factor and the velocity of the electron as dictated by the acceleration voltage. $\underline{A}$ and Φ are the vector and scalar potentials of the laser. We adopt the gauge where the scalar potential is zero and the high frequency photon oscillation negates the dot product term (besides being orthogonal). The vector potential of the laser beam is:

$$\underline{E}(\underline{r}, t) = \epsilon_0 \hat{y} g(y, z) \exp\left[-i\omega_L\left(t - \frac{x}{c}\right)\right] u\left(t - \frac{x}{c}\right)$$
$$\underline{A}(\underline{r}, t) = -\frac{\epsilon_0 \hat{y}}{\omega_L} g(y, z) \sin\left[\omega_L\left(t - \frac{x}{c}\right)\right] u\left(t - \frac{x}{c}\right)$$

with ϵ_0 as the field strength coefficient, c as the speed of light, ω_L as the frequency of the photon, g as the spatial distribution perpendicular to the travel direction, and u as the temporal distribution. Thus, the phase is:

$$\begin{aligned}
\phi(\underline{r}, t) &\approx -\frac{1}{\hbar}\frac{\epsilon_0^2}{\omega_L^2}\frac{e^2}{2m_e\gamma}\int dt' g^2(x, y, z) u^2\left(t' - \frac{x}{c}\right)\sin^2\left[\omega_L\left(t' - \frac{x}{c}\right)\right] \\
&= -\frac{1}{\hbar}\frac{\epsilon_0^2}{\omega_L^2}\frac{e^2}{2m_e\gamma}\int dt' g^2(x, y, z) u^2\left(t' - \frac{x}{c}\right)\left\{1 - \cos\left[2\omega_L\left(t' - \frac{x}{c}\right)\right]\right\}\frac{1}{2} \\
&\approx -\frac{1}{\hbar}\frac{\epsilon_0^2}{\omega_L^2}\frac{e^2}{4m_e\gamma}\int dt' g^2(x, y, z) u^2\left(t' - \frac{x}{c}\right)
\end{aligned}$$

We can assume the oscillatory sine and cosine terms do not contribute due to the high frequency oscillations of the photons. The laser pulse energy when integrated to infinity is given by:

$$\begin{aligned}
E_L &= c\varepsilon_0\epsilon_0^2\int_{-\infty}^{\infty} dt\, u^2(t)\cos^2(\omega_L t)\int_{-\infty}^{\infty} dydz g^2(y, z) \\
&\approx \frac{c\varepsilon_0}{2}\epsilon_0^2\int_{-\infty}^{\infty} dt\, u^2(t)\int_{-\infty}^{\infty} dydz g^2(y, z)
\end{aligned}$$

$$= \frac{c\varepsilon_0}{2}\epsilon_0^2 N_p$$

The shape of the laser pulse is described by a 2D spatial gaussian and a 1D temporal gaussian with the characteristic parameters for laser beam waist ω_0 and laser pulse duration τ_p. The normalization term is thus:

$$g_{00}^2(x,y,z) \propto \exp\left(-\frac{2(y^2+z^2)}{\omega_0^2}\right)$$

$$u^2(x,t) = \exp\left(-\frac{2\left(t-\frac{x}{c}\right)^2}{\tau_p^2}\right)$$

$$N_p = \frac{\omega_0^2\tau_p}{2}\sqrt{\frac{\pi^3}{2}}$$

Here, we will solely address the magnitude of the phase shift. The phase can be further simplified as:

$$\phi(\underline{r},t) \approx \frac{1}{\hbar}\frac{e^2}{\omega_L^2 m_e\gamma}\frac{E_L}{2c\varepsilon_0}\frac{\int dt' g^2(x,y,z)u^2(x,t')}{N_p} = \frac{1}{\hbar}\frac{e^2}{\omega_L^2 m_e\gamma}\frac{E_L}{2c\varepsilon_0}S(\underline{r},t)$$

$$= \frac{2\pi\alpha E_L}{\omega_L^2 m_e\gamma}S(\underline{r},t) = \frac{\alpha\lambda_L^2 E_L}{\gamma m_e c^2 2\pi}S(\underline{r},t) = \frac{\alpha\lambda_L^2 E_L}{2\pi E_e}S(\underline{r},t)$$

$$S(\underline{r},t)N_p = \int dt' \exp\left[-\frac{2}{\tau_p^2}\left(t'-\frac{x}{c}\right)^2\right]\exp\left[-\frac{2}{\omega_0^2}(z^2+y^2)\right]$$

By considering the positions (x,y,z) as functions of time for a traveling electron, the phase shift is:

$$\phi(\underline{r},t) \approx \frac{\alpha\lambda_L^2 E_L}{2\pi E_e}\frac{1}{N_p}\int dt' \exp\left[-\frac{2}{\tau_p^2}\left(t'-\frac{x}{c}\right)^2\right]\exp\left[-\frac{2}{\omega_0^2}(z^2+y^2)\right]$$

Phase is inherently difficult to measure. Instead, we measure the deflection caused by passing the electron through the laser beam. We expect the laser to roughly behave as a concave lens that is stronger in the axis perpendicular to the direction of laser travel. The momentum shifts are thus:

$$\delta\underline{p} = \hbar\nabla\phi(\underline{r},t)$$

$$\underline{\nabla}\phi(\underline{r},t) = \frac{\hbar\alpha\lambda_L^2 E_L}{2\pi E_e}\frac{\nabla\int dt' g^2(x,y,z(t'))u^2\left(t'-\frac{x}{c}\right)}{N_p}$$

$$= \frac{\hbar\alpha\lambda_L^2 E_L}{2\pi E_e N_p}\int dt'\underline{\nabla}\left[g^2(x,y,z)u^2\left(t'-\frac{x}{c}\right)\right]$$

$$\Delta p_x = \frac{\hbar\alpha\lambda_L^2 E_L}{2\pi E_e N_p}\int dt' \left\{\frac{4\left(t-\frac{x}{c}\right)}{c\tau_p^2}\exp\left[-\frac{2\left(t-\frac{x}{c}\right)^2}{\tau_p^2}-\frac{2(y^2+z^2)}{\omega_0^2}\right]\right\}$$

$$\Delta p_y = \frac{\hbar\alpha\lambda_L^2 E_L}{2\pi E_e N_p}\int dt' \left\{-\frac{4y}{\omega_0^2}\exp\left[-\frac{2\left(t'-\frac{x}{c}\right)^2}{\tau_p^2}-\frac{2(y^2+z^2)}{\omega^2(x)}\right]\right\}$$

1.2 Assumptions

Application of the equations above make the following assumptions of the experiment:

1. The laser and electron beams interact in such a small region relative to the travel distance of the electron beam that the momentum and phase shifts are instantaneously applied to the travel path of the electron beam. We have found this to be accurate in cases where the laser and electron pulse durations are at least shorter than 1 ns [2].

2. The gaussian beam profile has a best-fit to the fundamental transverse-electromagnetic (TEM_{00}) solution to the laser gaussian beam and ignores any fringes that may appear due to dust, mirror, or lens aberrations.

3. The photon oscillatory component (582 THz, ~1.7 fs period) truly plays no part on the timescales involved in the ponderomotive interaction (140 fs for the electrons to cross the interaction zone).

4. The effect can be averaged across varying electron pulse durations (due to fluctuations in electron counts) to be equivalent to an experiment performed at the average pulse duration.

1.3 Parameters used in simulations

In Figure 1 of the main text, we show a simulation that provides a reasonable match to the data collected by experiment. The properties of the electron beam and laser beam used in that simulation are described in the table below.

Table S1. Experimental parameters

Parameter	Used Value	Value Range
Magnification	15kx	10kx-20kx
Interaction to Sample	7000 µm	7000 µm[a]
Focus to Sample	-200 µm	0 to -630 µm[b]
Interaction Size	15 µm	12 to 24 µm[c]
Laser Bunch (s.d.)	212 fs	>212 fs[d]
Electron Bunch	6200 fs	5200 to 7200 fs[e]
Laser Focus	12.5 µm	12.4 to 12.6 µm[f]
Electron Focus	1 nm	>1nm[g]
Electron Rotation	-70º	-30º to -90º [h]
Electron Astigmatism (⊥/||)	0.5	0.25 to 0.75[h]
Electron Energy	30 keV	30 keV
Laser Pulse Energy	3.21 µJ/pulse	3.21 µJ/pulse[i]
Laser Wavelength	515 nm	515 nm[d]
Laser Positional Offset (⊥)	1.75 µm	1.75 µm[e]

[a]This is set by the position of the specimen stage
[b]This is the defocus range that the electron beam shifts by when moving from thermionic/Schottky mode to photoelectron mode
[c]As shown in Figure S2.
[d]Property of the laser, 500 fs fwhm
[e]As shown in Figure 2a of the main text
[f]As shown in Figure S1.
[g]Theoretical resolution limit of the SEM.
[h]As shown in Figure S2.
[i]Measured at a known position in the laser line

Laser Parameters

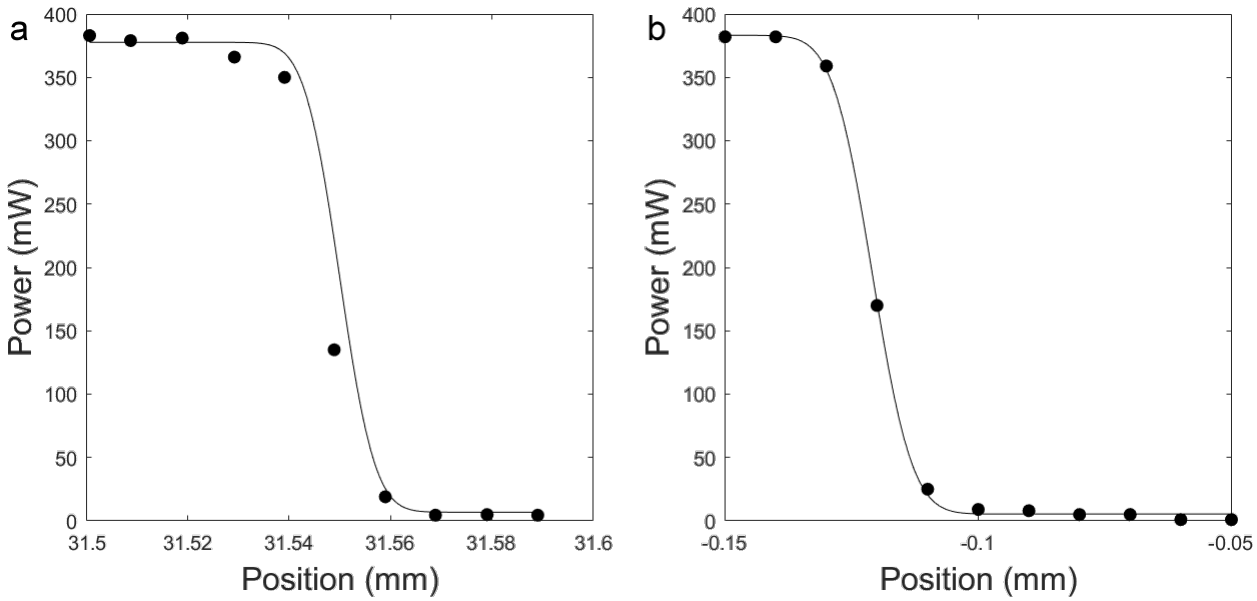

Figure S1. Size of the pump laser beam in the two directions perpendicular to the Poynting vector. Beam sizes are determined with a silicon knife edge within the microscope. **a,** The plot for the direction parallel to the electron beam. The size measured here is 12.6 microns. **b,** The plot for the direction perpendicular to both the Poynting vector of the laser and the electron beam. The size from the fit is 12.4 microns.

Electron Beam Parameters

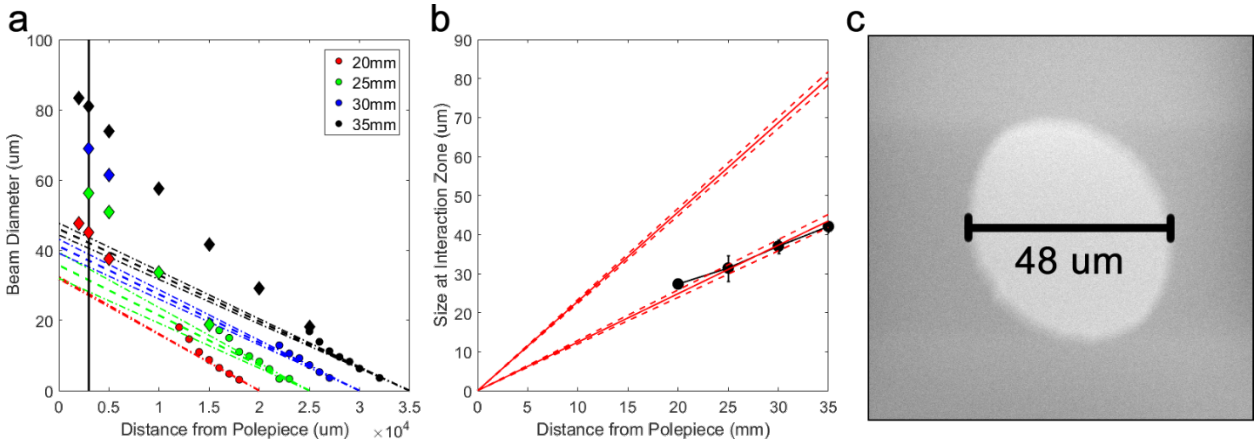

Figure S2. Size of the electron beam at various distances from the focal point. a, The electron beam ideally linearly increases in size as it moves further away from the working distance (focal point). The working distance is set to a specific position (indicated by color) and measurements of the beam size are acquired by imaging a small piece of dust and dividing the resulting size dimensions by a factor of two. These dimensions are plotted as a function of distance from the polepiece. **b,** When the 1000 micron aperture is used, the size of the electron beam in the interaction region (7 mm) is 12 to 24 microns. These two values are derived from the information found by the non-linear data (**a**) split into a far-field set and a near-field set. The true beam size must be intermediate in value. This value is used in the simulations (see Supplementary Note 1 and Supplementary Table S1). **c,** A description of the electron beam size 3mm from the polepiece. The true size of the electron beam must be divided by a factor of two.

Control experiment

To ensure the effect we observed was central to the interaction region between the laser and the electron beam, we performed an additional control. The specimen was moved 23.5 mm away from the interaction zone. If the observed effect was dependent on the surface of the specimen, then the time-zero position[3,4] would move. Here, we observed no difference in time-zero, ensuring that the effect we observed is localized to the laser-electron interaction zone.

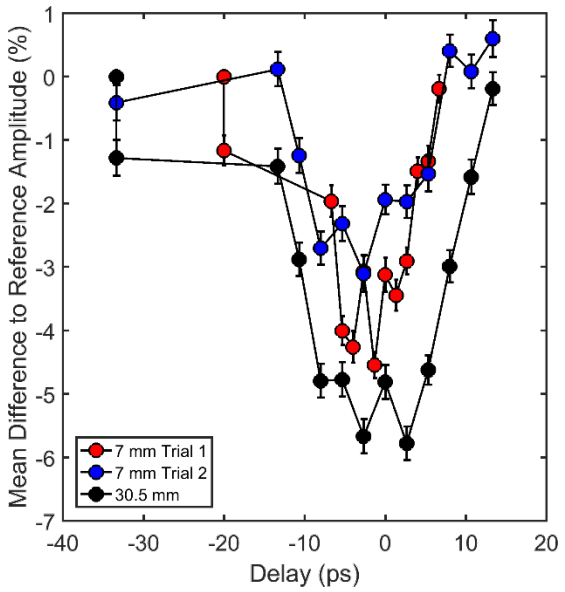

Figure S3. Interaction control to ensure no surface effect. The same trials from the 0.5 nJ/pulse experiments from Figure 2 of the main text are repeated here, including the reference images. A third experiment involving the moved specimen set to 30.5 mm away from the polepiece is also overlayed on the image. We can see that t_0 has not moved by an expected 23.5 mm on the delay stage (more than 100 ps).

References

1. Mihaila, M. C. C., *et al*. Transverse Electron Beam Shaping with Light. *Phys. Rev. X* **12**, 031043 (2022).
2. Du, D. X. & Fitzpatrick, A. W. P. Design of an ultrafast pulsed ponderomotive phase plate for cryo-electron tomography. *Cell Reports Methods* **3**, 100387 (2023).
3. Yang, D.-S., Mohammed, O. F. & Zewail, A. H. Scanning ultrafast electron microscopy. *Proc. Natl. Acad. Sci.* **107**, 14993-14998 (2010).
4. Du, D. X., *et al.* Development of an ultrafast pulsed ponderomotive phase plate for cryo-electron tomography. *bioRxiv* 2024.03.20.585981 (2024).